

INVITED PAPER

PACS numbers: 42.55.Px; 42.60.Lh; 78.67.De
DOI: 10.1070/QE2012v042n10ABEH014910

Active-region designs in quantum cascade lasers

I.I. Zasavitskii

Abstract. **This paper analyses the development of active-region designs in quantum cascade lasers. Active-region designs have been demonstrated to date that employ various radiative transitions (vertical, diagonal, interminiband and interband). The lower laser level is depopulated through nonradiative transitions, such as one- or two-phonon (and even three-phonon) relaxation or bound state → continuum transitions. Advances in active-region designs and energy diagram optimisation in the past few years have led to significant improvements in important characteristics of quantum cascade lasers, such as their output power, emission bandwidth, characteristic temperature and efficiency.**

Keywords: *quantum cascade laser, quantum well, barrier, radiative and nonradiative transitions, characteristic temperature, optical power, efficiency.*

1. Introduction

The idea that electromagnetic waves can be amplified in a semiconductor with a superlattice (SL) was put forward in 1971 [1], and the first unipolar quantum cascade laser (QCL) was demonstrated in 1994 [2]. An essential point was that scattering with the participation of a longitudinal optical (LO) phonon was added to the QCL scheme. As a result, a four-level laser system was obtained. A typical QCL includes a periodic arrangement of active regions (~30) and adjacent injectors. Each active region of a QCL is a heterostructure consisting, as a rule, of three tunnelling-coupled quantum wells of depth $U_0 = \Delta E_c = 0.3–2$ eV and width 1–6 nm, where ΔE_c is the conduction band offset. The upper laser level is pumped through tunnelling injection in an electric field, and the lower laser level is depopulated through resonant LO phonon–electron scattering. To date, active-region designs have been proposed with various radiative transitions, namely, vertical transitions within a quantum well, diagonal transitions between quantum wells, interminiband transitions in the SL and diagonal interband transitions between quantum wells in the conduction band and valence band. The lower laser level is depopulated through nonradiative transitions, such as one- or two-phonon (and even three-phonon) relaxation or bound state → continuum transitions and their combinations. Owing to recent advances in the technology of QCLs, devices are now available for the spectral range 4–12 μm that operate in continuous mode at room temperature and offer output powers above 0.1 W. Advanced design strategies have enabled QCLs with record-high performance to be created.

This paper addresses the development of active-region designs in QCLs based on epitaxial nanoheterostructures. 'Active region' is here taken to mean several (three to six) tunnelling-coupled quantum wells under bias. Each active region has an injector. It is shown how advances in active-region designs and energy diagram optimisation in the past few years have led to significant improvements in important characteristics of QCLs, such as their output power, emission bandwidth, characteristic temperature and efficiency.

I.I.Zasavitskii P.N. Lebedev Physics Institute, Russian Academy of Sciences, Leninsky prosp. 53, 119991 Moscow, Russia;
e-mail: zasavit@sci.lebedev.ru

Received 14 June 2012
Kvantovaya Elektronika **42** (10) 863–873 (2012)
Translated by O.M. Tsarev

2. Schemes of transitions in QCLs

Let us recall briefly the operating principle of a QCL under bias [3]. Figure 1 shows a typical diagram of a radiative and a nonradiative transition in a QCL containing three quantum wells in its active region. Here, E_3 and E_2 are the upper and lower laser level energies, the difference between which determines the emitted photon energy ($h\nu = E_3 - E_2$). The active-region design ensures that $E_2 - E_1 \geqslant h\nu_{LO}$. As a result of tunnelling injection through the first barrier, an electron from the injector reaches the level in the first well and then level 3 in the second well. Next, it undergoes a transition to level 2 in the same well, emitting a photon, and then a transition to level 1 in the third well, emitting a longitudinal optical (LO) phonon. From this well, it tunnels into the injector of the next stage, where the process is repeated.

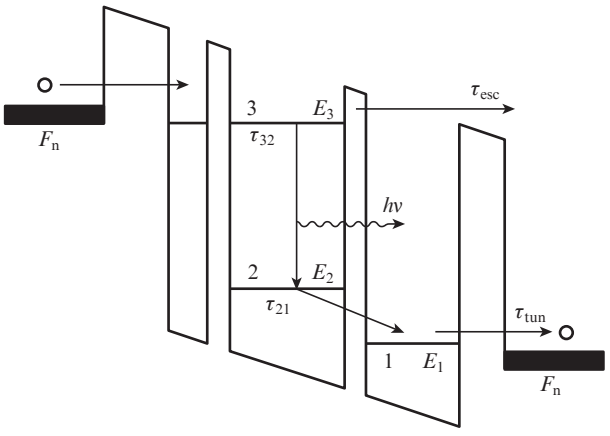

Figure 1. Typical band diagram of an active region with resonant one-phonon depopulation of the lower laser level [4]. F_n is the Fermi level.

In the case of intersubband transitions, Auger recombination is suppressed to within the subband nonparabolicity. Since an epitaxial heterostructure is a combination of pure materials, the dominant mechanism of carrier scattering in the active region is interaction with a longitudinal optical (LO) phonon. Scattering from level 3 requires 'exchanging' a large wave vector, whereas the transition from level 2 to level 1 has a resonance character, i.e. is more efficient. As a result, the lifetime at level 3 ($\tau_{32} \sim 2-5$ ps) is an order of magnitude longer than that at level 2 ($\tau_{21} \sim 0.2-0.4$ ps). The ratio of these lifetimes is determined by the specifics of a particular design scheme. Thus, in the case of two specially engineered, tunnelling-coupled quantum wells a certain applied electric field leads to population inversion. Pumping to the upper laser level 3 and depopulation of level 1 are ensured by tunnelling injection over a time $\tau_{tun} \sim 0.2$ ps. Another important parameter of QCLs is the carrier lifetime for radiative recombination. It is relatively long ($\sim$1 ns), so the internal quantum yield of emission for the optical transition under consideration is low ($\sim 10^{-3}$). To increase it, cascade designs are used. A typical number of stages is 30–40, but there are designs with both one stage and a larger number of stages (about 100). Note that, under certain conditions, cascading enables a differential quantum yield $\eta_{dif} > 1$ to be reached.

The main task in producing a population inversion – to ensure the highest possible upper level pumping efficiency and rapid lower level depopulation – is accomplished in QCLs as follows: The first narrow quantum well, containing only one level, serves to further localise the electron wave function and reduce the probability of nonradiative transitions to level 2. This ensures efficient injection. To reduce the leakage current, the active region should be engineered so that the other high-energy levels in the second and third wells lie far enough from the upper laser level. Moreover, electrons should be incapable of directly tunnelling from the upper level to the injector (over a time $\tau_{esc} \sim 15$ ps), which is ensured by the injector minigap. The injector is a slightly chirped, partially doped SL. It serves the following functions: (1) it acts as an electron reservoir and contributes to electron cooling, (2) it precludes domain formation in an electric field, and (3) it forms a minigap which blocks parasitic transitions from the upper laser level. The energy difference between the lower laser level and the ground level of the injector is a measure of backfilling. This difference determines the voltage defect, V_{def}, which reflects the difference between the voltage drop across each stage, V_{stage}, and the emitted photon energy divided by the electron charge: $V_{def} = V_{stage} - h\nu/e$. To raise the operating temperature of a QCL, one should increase the voltage defect, but this will be accompanied by a drop in laser efficiency.

The optical transitions between the upper and lower laser levels in real space can be vertical (within a particular quantum well) and diagonal (Fig. 2a). This means that diagonal transitions occur between different – usually neighbouring – quantum wells. Their advantage is that they have a large transition dipole moment: up to 2 nm for vertical transitions and up to 4 nm for diagonal transitions. However, because of the interface scattering, the electroluminescence (EL) linewidth for diagonal transitions is also markedly larger. At low temperatures, the smallest linewidth was about 10 and 20 meV for vertical and diagonal transitions, respectively. At 300 K, the linewidth is larger by about a factor of 2 and of course depends on the scheme of transitions. In special cases, it can reach much higher values. Figure 2b shows three diagrams of optical transitions: from a discrete state to a continuum and from a doublet ($\sim$10-meV splitting) to a discrete state or continuum. It is in the last case that a large EL linewidth was observed: at least 60 meV (500 cm^{-1}) [5].

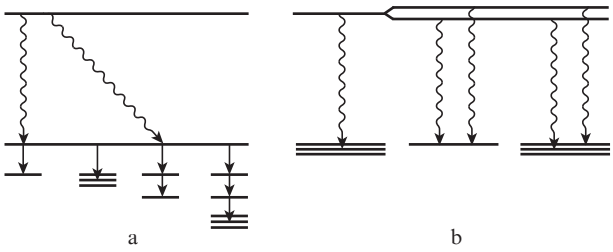

Figure 2. Diagrams of transitions in QCLs. The wavy arrows represent radiative transitions.

Also shown in Fig. 2a are nonradiative transitions involving an LO phonon that depopulate the lower laser level. Nonradiative transitions may involve one [2, 3], two [6] or even three [7] LO phonons. Because designs with a large number of resonant phonon transitions are difficult to tune, use is often made of transitions from a lower laser level to a continuum [6]. Sometimes, a combination of transitions is employed: e.g. a one-phonon transition plus a bound state → continuum transition. These design complexities are intended to reduce (by a factor of 2 or more) the lower laser level lifetime. Note that the phonon bottleneck problem can be solved in a similar way in the case of the radiative transitions shown in Fig. 2b.

In what follows, before analysing recent advances in QCLs, we briefly discuss two active-region designs of special interest: SL-based and interband QCLs.

2.1. SL-based active region

In Fig. 2b, one can see a tendency towards broadening (participation of a few quantum states) of both the upper and lower laser levels. In some limit, this leads to the formation of minibands of allowed states, typical of SLs. Such interminiband transitions were demonstrated as early as at the beginning of QCL development [8]. An interminiband QCL is also a unipolar device and takes advantage of optical transitions between SL minibands.

A superlattice is a periodic structure made up of alternating nanometre-thick layers of two semiconductor materials differing in bandgap, one of which plays the role of a quantum well and the other acts as a barrier. The period ($d \sim 5$ nm) of such a man-made crystal is typically greater than the lattice parameters ($a \sim 0.5$ nm) of the constituent materials. An applied potential splits its conduction and valence bands into narrow minibands and minigaps along the normal to the layers.

In the strong tunnelling coupling regime, where the barrier width is 1–2 nm, the minibands and minigaps range in width from tens to hundreds of millielectronvolts. If an SL is undoped or slightly doped (to at least 10^{17} cm^{-3}), the Fermi level (at least 10 meV) is situated at the bottom of the first miniband, i.e., the upper part of the miniband, $\sim$100 meV in width, remains empty. Electrons are injected near the bottom of the second miniband and can then pass to the top of the first miniband, emitting a photon (Fig. 3). An important point is that their lifetime is determined by scattering from high-

momentum optical phonons and is ~10 ps. Within a miniband, relaxation occurs with a low momentum, so the relaxation time is just tenths of a picosecond. This large ratio of the interminiband and intraminiband relaxation times ensures population inversion in wide ranges of quantum-well and barrier widths, which allows large optical transition matrix elements to be reached through optimisation. Eventually, interminiband QCLs offer a higher current carrying capability and, hence, higher output power. Another advantage of QCLs is the ease of achieving population inversion – due to the large ratio of the interminiband and intraminiband relaxation times – and a high oscillator strength of the laser transition on the boundary of the Brillouin zone of the SL. The oscillator strength increases with decreasing barrier thickness.

To minimise the external-field penetration into the SL and suppress the space charge effect on the injection process, doping of the SL is used. Doping maintains a flat band profile in the SL and allows one to avoid breakdown of the minibands under external bias. At the same time, doped-SL QCLs have relatively low performance because electrons are scattered by the dopant and photons are absorbed by free carriers, which is particularly essential for long-wavelength lasers. In connection with this, a QCL was proposed with special doping in the injector region. This approach enabled a decrease in threshold current and an increase in 300-K output power.

A record-high performance of QCLs was achieved when a purpose-designed, undoped SL was used in the active region. In such an SL, an external field is compensated by an internal quasi-electric field resulting from a gradual variation in the period and average elemental composition of the SL. Figure 3 schematically shows such an SL, an injector and interminiband optical transitions. The thicknesses of the layers in the heterostructure are as follows (from right to left in Fig. 3): **3.5**/*5.1*/***1.1***/*4.8*/***1.1***/*4.4*/***1.1***/*4.1*/***1.2***/*3.8*/***1.3***/*3.5*/***2.5***/2.3/**2.5**/2.3/**2.5**/2.2/**2.6**/2.0/**2.6**/1.9/**2.7**/1.9/**2.9**/1.8 nm. The thicknesses of the $Al_{0.48}In_{0.52}As$ barriers, starting from the injection barrier, are indicated in bold type, the thicknesses of the $Ga_{0.47}In_{0.53}As$ quantum wells are set in roman type, and those of the layers in the SL active region are in italics. The thicknesses of the injector layers doped to 2×10^{17} cm^{-3} are underlined. Like the injector, the SL in this QCL is a smooth chirped structure. In both the active region and injector, the SL period varies so as to obtain a horizontal arrangement of the minibands at an applied electric field (E = 45 kV cm^{-1}). The best results were obtained [9, 10] for flat-miniband QCLs, i.e. SL QCLs in which the applied field is compensated by the internal field. Such QCLs offer a high current carrying capability and oscillator strength, which eventually has resulted in high optical powers (~1 W) and high operating temperatures (300 K or above) of long-wavelength (7–17 μm) lasers. Note however that the growth of such heterostructures, where many of the layers are only a few monolayers thick, poses serious technological problems.

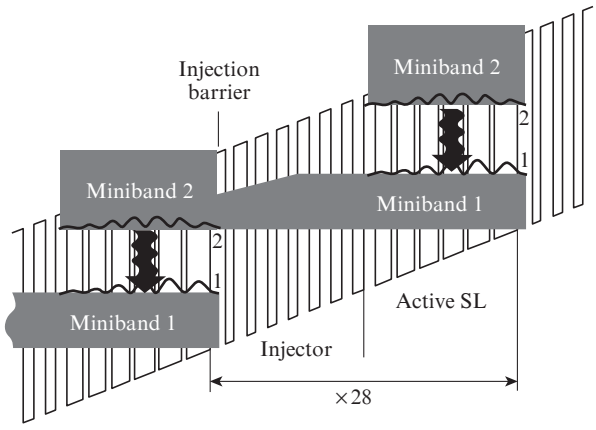

Figure 3. Band diagram of an interminiband QCL [9, 10].

2.2. Interband QCL

Above we considered an active region created in one of the bands, namely, in the conduction band. Since the energy spectrum is quantised as well in the valence band, the spectrum here is discrete and is determined by the hole effective mass. Consider now a system of two coupled quantum wells that form a type II heterojunction, where the valence band top in the second well is located higher than the conduction band bottom in the first well. A classic example is the InAs/GaSb system, which possesses semimetallic properties because of such band overlap. In the case of size quantisation, however, the valence band top in GaSb and the conduction band bottom in InAs are farther apart (the degeneracy is lifted), and the InAs/GaSb system is an insulator. Since the wave functions of an electron in InAs and a hole in GaSb overlap, there is an appreciable probability of their radiative recombination. Such an interfacial radiative transition between discrete levels of a type II heterojunction is used in interband QCLs [11, 12]. Figure 4 shows a simplified band diagram of the active region in an interband QCL.

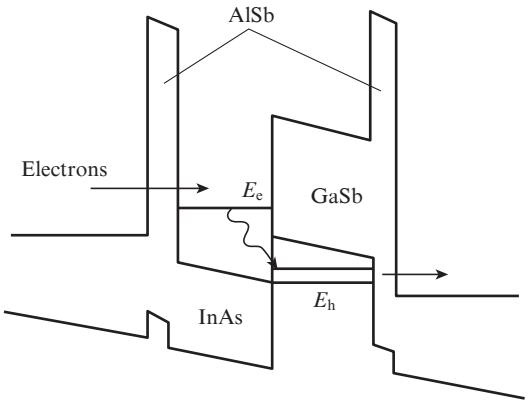

Figure 4. Simplified band diagram of the active region in an interband QCL.

It is worth noting that the structure utilises a third material: AlSb. The InAs/AlSb system is of interest in that it has a very large conduction band offset ($\Delta E_c \approx 2$ eV) and electrons in InAs have a low effective mass, which leads to strong quantisation. It is seen in Fig. 4 that electrons tunnel from the injector through a thin AlSb barrier to the lower quantum level in InAs (energy E_e). Next, the electrons recombine radiatively with holes at the level of energy E_h in the valence band of GaSb (GaInSb solid solutions are also often used). After that, an electron is captured at another hole level in GaSb through a tunnelling process, with emission of a longitudinal optical phonon. The electron then reaches the injector, and

the process is repeated in the next stage. One distinction from the intraband QCL design is that the electron was twice in the valence band, even though eventually it was located again in conduction band of the injector. For this reason, the interband QCL is also a unipolar device.

The interband QCL has the following advantages. Since the relaxation of nonequilibrium electrons is an interband process (transition between levels at E_e and E_h), its rate is slower than that of the intraband phonon-assisted relaxation between quantum levels. This makes it easier to pump the system and produce an inverse population. Moreover, using bandgap engineering, one can considerably suppress Auger recombination.

Even though the interband QCL was proposed long ago [11, 12] and has been the subject of intense attention, mainly from a group at the U.S. Naval Research Laboratory (Washington, DC) [13–15], the laser performance achieved is lower than that predicted theoretically and is significantly inferior to that of intraband QCLs. This is primarily because the InAs/AlSb, InAs/GaSb and GaSb/AlSb systems are poorly lattice-matched, and the epitaxial growth of such heterostructures has not yet been sufficiently developed. It is also worth noting that these materials contain high defect densities and have active surface recombination. Moreover, the interband QCL design requires further optimisation. Consider key achievements in the field of interband QCLs.

In pulsed mode, interband QCLs have demonstrated a high optical power (over 4 W per facet) and relatively high operating temperature (up to 217 K) [16]. Their threshold current density is, however, much higher than that predicted theoretically. In continuous mode, an optical power above 1 W at $T = 78$ K has been obtained [13]. Currently, interband QCLs offer more than 10 mW of cw output power above room temperature [14, 15]. In contrast to classic QCLs, which operate at wavelengths longer than 4 μm, interband QCLs emit in the spectral range 3–4.2 μm. Note that, even though interband QCLs have a markedly lower output power, they have a lower threshold current, which increases their reliability.

Consider now design schemes that have enabled significant improvements in the performance of typical QCLs.

3. Temperature dependence of the threshold current density

It is known that the temperature dependence of the threshold current density for semiconductor lasers can be represented by the empirical formula

$$J_{th}(T) = J_0 \exp(T/T_0), \tag{1}$$

where T_0 is a characteristic temperature dependent on the type of laser. The characteristic temperatures of the best homojunction laser, heterostructure laser and QCL are 50, 100 and 200 K, respectively. At the same time, recent work has shown that the T_0 of QCLs can be considerably higher, up to 500 K, which corresponds to a very weak temperature dependence of the threshold current. This can be accounted for by the fact that Auger recombination in QCLs is suppressed because these are unipolar devices with intersubband transitions. For this reason, they offer higher T_0 than do conventional mid-IR interband lasers. The characteristic temperature T_0 reflects the temperature effect on the carrier distribution, carrier scattering time and optical gain mechanism. In contrast to conventional diode lasers, QCLs open up the possibility of tuning these characteristics through bandgap engineering of the energy spectrum and carrier distribution probability. There is often a complex relationship between different components of a heterostructure, which leads to a compromise solution. Consider some reports that address this issue.

Huang et al. [17] employed a diagonal optical transition to reduce the overlap between the upper and lower laser levels and increase the electron lifetime at the upper laser level U (Fig. 5). Moreover, in their approach the upper laser level 'penetrates' deep into the injector region, enabling efficient electron injection through both resonant tunnelling from the injector ground level and phonon-assisted scattering from higher injector levels. The lower laser level (I) is depopulated according to a 'two-phonon-continuum' scheme. In this scheme, an electron at the lower laser level (I) is scattered, with emission of an LO phonon, to another, lower energy level (II) and then is scattered, emitting an LO phonon, to one of the levels of a lower energy continuum. This scheme combines the advantages of the two-phonon resonance design [18] and bound-to-continuum design (fast electron extraction from the active region to the injector through a miniband [19]) and is similar but not identical to the existing single-phonon resonance–continuum depopulation scheme [20], in which the exit barrier should be designed carefully to suppress the extension of wave functions from the injector miniband to the active region and obtain a bound-to-bound optical transition. In the 'two-phonon-continuum' scheme under consideration, the entire injector miniband 'penetrates' deep into the active region and below level II to form a wide (~70 meV) continuum, which results in efficient electron extraction to the injector and fast electron transport to the upper laser level in the next active region (stage). At the same time, the bound-to-bound lasing transition is retained because the continuum is well below the lower laser level and level II. To prevent thermal backfilling of electrons to the lower laser level, the separation between the lower laser level and injector ground level is made as large as ~150 eV. To suppress electron leakage, the next upper level in the active region (UU) is ~63 meV above the upper laser level (I).

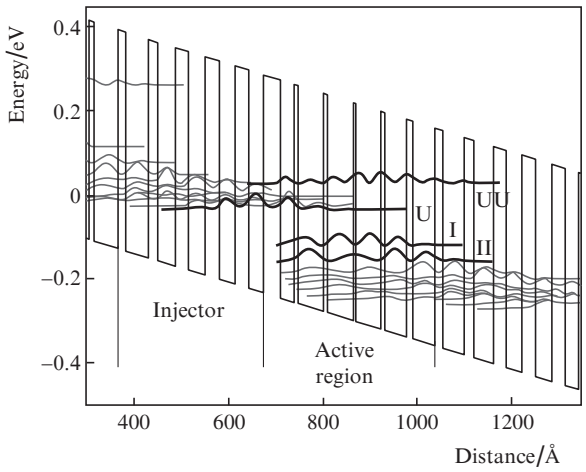

Figure 5. Band diagram of a QCL with a diagonal optical transition and 'two-phonon-continuum' depletion of the lower laser level; $\lambda \sim 14$ μm, $T = 300$ K, $E = 35$ kV cm^{-1} [17].

As shown above, design optimisation is intended to achieve efficient electron injection and extraction and reduce the leakage current and thermal backfilling of charge carriers. Owing to design optimisation, a high characteristic temperature T_0 was obtained. Using (1), we obtain $T_0 = 189$ K in the temperature range 80–240 K and $T_0 = 306$ K in the range 240–390 K. The increase in T_0 with temperature can be explained by the temperature variation of the energy difference between the lower laser level and the level just below it. The energy separation increases with temperature and exceeds the LO phonon energy at $T > 240$ K. This leads to a higher depletion rate of the lower laser level by one-phonon scattering. As a result, the one-phonon-assisted scattering time decreases from ~0.4 s below 240 K to 0.2 ps or less above 240 K. The higher depopulation rate of the lower laser level leads to partial compensation of thermal backfilling and a slower increase in threshold current with temperature for $T > 240$ K.

Fujita et al. [5] proposed a broad-gain QCL design, which they referred to as 'the dual-upper-state to multiple-lower-state (DAU/MS) transition design'. It includes (Fig. 6) two coupled split upper laser states of the same type, in which the wave function shape and energy separations can be well optimised to give desired electron populations and nearly equal strengths of the transitions from the two upper levels. In addition, they are energetically separated from higher parasitic states to ensure selective injection into the two upper states. Optical transitions occur from the dual upper state to the lower state (continuum). This carefully designed configuration of the DAU/MS laser led to the development of devices with peculiar characteristics: a broad, symmetric EL band, weak voltage dependence of the EL linewidth, very high T_0 and superlinear light–current behaviour. Fujita et al. [5] demonstrated a broad-gain QCL with an extremely weak temperature dependence of the threshold current ($T_0 \sim 510$ K).

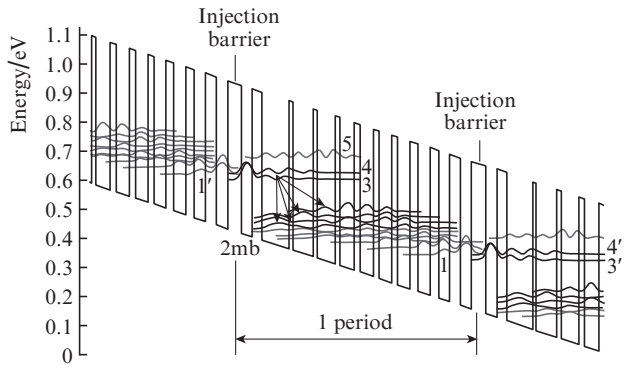

Figure 6. Conduction-band diagram and modulus-squared wave functions for an injector–active region–injector structure at an applied electric field $E = 41$ kV cm^{-1} [5].

Figure 6 shows the conduction-band diagram for three regions: injector, active region and injector. The two coupled upper states are labelled 4 and 3. When a voltage is applied, electrons are injected into the upper state 4 via resonant tunnelling from the ground level 1′. According to Fujita et al. [5], it is the proximity in energy of level 1′ to level 4 (not to level 3) that is responsible for the broad gain band. In this situation, electrons are rapidly distributed between the two upper laser states via longitudinal optical phonon assisted scattering and/or electron–electron scattering. Such fast relaxation processes are very important for eliminating dynamic spectral hole burning above lasing threshold. The two upper laser levels have essentially identical electron populations because of the small energy separation between them ($E_{43} \sim 20$ meV). On the other hand, the lower laser states form a miniband (labelled 2mb), in which the wave functions extend over the entire active region and injector. Thus, in this design transitions occur from states 4 and 3 to the 2mb miniband, and the large number of channels for transitions leads to a broad gain band. The energy separation between the upper laser states and parasitic state 5 is made as large as possible ($E_{54} \sim 60$ meV) to ensure high T_0 and superlinear light–current behaviour.

Estimates by Botez et al. [21] suggest that, to raise the characteristic temperature T_0, one should reduce the leakage current to higher energy states, which can be achieved by increasing the quantum-well depth and barrier height. Bai et al. [22] demonstrated another approach, with the use of shallow, asymmetric quantum wells. They introduced several design elements which reduced the temperature sensitivity of the QCL without preventing it from having high efficiency at room temperature.

Figure 7 illustrates the shallow-well QCL design proposed in that study. This structure incorporates five different materials. The AlAs inserts in the injector region are intended to minimise carrier leakage into the continuum, i.e. the active region wave functions in this structure are more confined, and their coupling to the continuum states is reduced. In contrast to the deep-well design, where the active region is composed of deep wells and high barriers, this design has a shallow well and low barrier in the active region. The structure was simulated near the rollover voltage in its voltage–current curve, where the upper laser level (level 3) aligns with the injector ground level (level g) of the previous stage. The voltage defect at the corresponding field strength, given by the energy difference between the lower laser level and injector ground level, is 180 meV, which is slightly higher than that in typical QCL designs (~160 meV) at a similar wavelength.

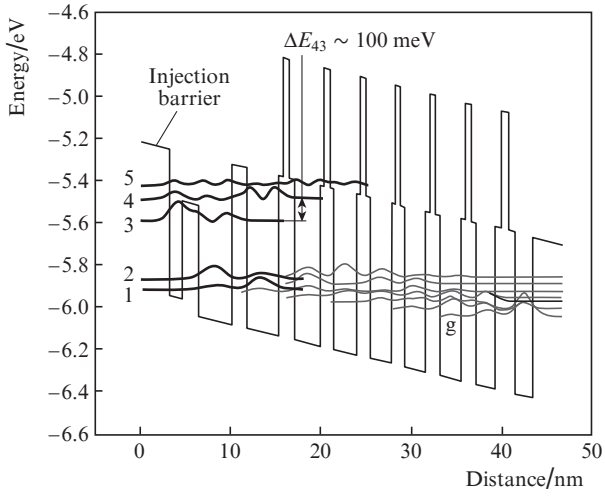

Figure 7. Conduction-band diagram and modulus-squared wave functions for the shallow-well design ($Ga_{0.47}In_{0.53}As/Al_{0.48}In_{0.52}As$ system) at $E = 105$ kV cm^{-1}. The heterostructure is formed by $Ga_{0.31}In_{0.69}As/Al_{0.64}In_{0.36}As$, with AlAs inserts in the injector barriers for reducing carrier leakage into the continuum [22].

As pointed out by Hofstetter et al. [18], the main contribution to carrier leakage, which leads to low characteristic temperatures, is through LO-phonon scattering from level 3 to level 4. The close-to-lattice-matched materials in the active region serve to minimise carrier leakage to levels above the upper laser level, which is achieved by considerably increasing the energy separation between levels 3 and 4. Compared to the conventional design without such materials, ΔE_{43} is increased from 80 to 100 meV. Note that 80 meV corresponds to a conventional design with a three-well active region, i.e. with a single-phonon resonance. In the case of a four-well design, i.e. two-phonon resonance, this energy separation is even smaller (~46 meV).

In addition, the shallow-well design reduces interface roughness scattering, which is known to markedly increase the luminescence linewidth of QCLs. Since the first well and barrier in the active region considerably overlap with the upper laser level in the case of a diagonal design, the use of small band offset materials ensures a decrease in interface roughness scattering.

In conclusion, Table 1 lists the characteristic temperatures T_0 reached to date for various QCL designs, along with their emission wavelengths, threshold current densities and optical pulse powers at $T = 300$ K. The characteristic temperature of the QCLs operating in the spectral range 5–15 μm has been considerably raised ($T_0 = 300–500$ K), primarily by reducing the leakage current to higher energy parasitic states and also by using two- and three-step backfilling, incorporating high AlAs barriers into the injector and reducing interface roughness scattering.

Table 1. Emission wavelength, threshold current density and optical pulse power at $T = 300$ K and characteristic temperature T_0 for various QCL designs.

Design	λ/ μm	J_{th}/ kA cm^{-2}	P/ W	T_0/ K	Temperature range/K
Shallow well and AlAs layers in the injector to minimise leakage [22]	5	1.43	–	383	298–373
Dual upper laser level → continuum [5]	8.7	2.6	~1	510	300–400
Diagonal transition + 2 LO phonons → continuum [17]	14	2.0	0.336	306	240–390
Diagonal transition with an intermediate state + 1 phonon [23]	15	3.5	–	450	320–380

4. Extension of the spectral range and continuous frequency tuning of QCLs

The emission wavelength of QCLs is in principle easy to tune by varying their design parameters (band offset, i.e. the quantum well depth and width and effective mass), and this advantage of QCLs was highlighted in many reports, with particular emphasis on the quantum well width. In practice, however, only a small number of technologically viable material systems are capable of simultaneously meeting requirements such as a good lattice match, large band offset and small effective mass. Basically, key achievements have been made in two material systems: GaInAs/AlInAs and GaAs/AlGaAs. This has made it possible to cover spectral regions in the mid-IR (3.3–24 μm) and far-IR (67–250 μm). The use of the less technologically attractive system InAs/AlSb enabled extension to shorter wavelengths, down to 2.6 μm [24]. The antimony-containing solid solutions are expected to cover the range 2.6–4 μm. At the same time, the 1.5-μm and visible ranges, which are of great practical importance, remain to be covered. A search is already under way for other material systems, primarily with large band offsets, e.g. nitrides. Without dwelling on this point, it is worth indicating the difficulties one has to face on the way to shorter wavelengths: (1) Carrier leakage to higher energy states and, eventually, to the continuum increases because of the thermal activation. (2) In III–V semiconductors, there is intervalley scattering to the X and L side valleys, which increases with photon energy. (3) There is resonance reabsorption in the carrier extraction region. (4) Quantum well narrowing toughens the requirements for interface quality and stress control during growth. (5) The operating voltage increases with photon energy, i.e. heat removal from QCLs becomes a more serious problem at a relatively low efficiency.

The main problems in the case of the long-wavelength QCLs differ from those with the short-wavelength lasers: (1) Considerable population inversion is more difficult to achieve because the upper laser level lifetime decreases with decreasing optical-transition energy by virtue of the higher LO-phonon-assisted scattering rate. (2) Leakage from the injector directly to the lower laser level is higher. (3) The lower photon energy leads to a lower voltage efficiency (the ratio of the photon energy to the total energy per stage). (4) The waveguide loss is higher because absorption by free carriers is roughly proportional to the square of the emission wavelength. For a given quantum-well material, the longitudinal optical phonon energy determines the long-wavelength limit of QCL operation. For the $Ga_{0.53}In_{0.47}As$ solid solution ($h\nu_{LO}$ = 35 meV), the longest lasing wavelength is 24 μm [25].

An important issue is the ability to extend the spectral range of QCL operation. For practical applications (especially for high-resolution molecular spectroscopy, high-sensitivity spectral gas analysis, and optical heterodyning), continuous, i.e. single-mode, laser wavelength tuning in as wide a spectral range as possible is needed. There are several ways of achieving single-mode operation. One standard approach for semiconductor lasers is the use of distributed feedback. Like in the case of other types of diode lasers, distributed-feedback QCLs were demonstrated and single-mode frequency tuning through temperature variations was achieved in the range 10–20 cm^{-1}, with a side mode suppression ratio of 30 dB [26]. This approach is traditional and gives a relatively narrow tuning range. The unique feature of QCLs is that their gain bandwidth can be significantly increased and that, using an external dispersion cavity, one can tune the single-mode frequency in a wide range [27]. Given below are several examples.

The idea of creating a QCL with several active subregions, each tuned to its own emission wavelength, and, eventually, the idea of creating an ultrabroadband laser were realised by Gmachl et al. [28, 29]. As shown later [30], a grating-coupled external cavity laser is capable of single-mode operation with a mode-hop-free tuning range of width Δk = 155 cm^{-1}. The tuning range was increased to 432 cm^{-1} by using an active region incorporating five subregions [31], in which bound-to-

continuum transitions occurred and which were each tuned to a particular optical-transition energy. The five subregions form a broad EL band. The EL line is asymmetric and its width decreases with increasing applied voltage. The single-mode range of the QCL was 7.6–11.4 μm.

Of special note is that the EL bandwidth in QCLs can be increased not only by producing heterogeneous active regions but also by using transitions that broaden the EL line. Yao et al. [32] used continuum-to-continuum optical transitions due to strong coupling between the active region and adjacent injectors and obtained a broad EL band ($\Delta k \sim 430$ cm^{-1}, $\lambda \sim 4.8$ μm, $\Delta\lambda/\lambda \sim 0.2$). Fujita et al. [5] employed DAU/MS transitions, i.e. dual-state to continuum transitions. They obtained a very broad ($\Delta k \sim 500$ cm^{-1}, $\lambda \sim 8.7$ μm, $\Delta\lambda/\lambda \sim 0.4$), asymmetric EL line with a weak voltage dependence of its width. Later, the EL linewidth was increased to 600 cm^{-1} [33].

Thus, there are great possibilities for creating widely tunable single-mode QCLs.

5. Record-high output powers

As mentioned above, currently a typical 300-K output power of mid-IR QCLs in the spectral range 4–12 μm is up to 0.1 W in continuous mode and several watts in pulsed mode. At the same time, an order of magnitude higher power levels have recently been reached by optimising the QCL design and improving post-growth processing (cavity length, high-reflection-coated back facet, antireflection-coated front facet, improved heat removal conditions). Such QCLs have been demonstrated mainly by researchers at Northwestern University (Illinois, USA) and Pranalytica, Inc. (California, USA).

At Northwestern, laser heterostructures are commonly grown by gas-source molecular beam epitaxy. The latest advances in QCLs are related to the shallow-well design [22, 34], more strictly, to the three asymmetric well design considered above. Recall that, in this design, the injector region contains AlAs inserts. This design allows one not only to obtain high T_0 but also to reduce the leakage current and raise the output power. Moreover, the shallow-well design experiences reduced interface roughness scattering for the lasing transition, which is known to make a major contribution to the EL line broadening in QCLs. Bai et al. [34] obtained a single-facet cw output power of 5.1 W at a wavelength of 4.9 μm and $T = 300$ K (buried-ridge device, 40 stages, cavity length of 5 mm, ridge width of 8 μm, high-reflection and antireflection coated facets, diamond submount). The wall plug efficiency was 21% and 27% in continuous and pulsed modes, respectively.

Currently, the single-mode output power of distributed-feedback lasers reaches ~0.1 W. Using a strain-balanced $Ga_{0.331}In_{0.669}As$/ $Al_{0.638}In_{0.362}As$ structure, Lu et al. [35] produced a distributed-feedback QCL which utilised vertical radiative transitions and two-phonon resonant depopulation (four-well active region) [18]. Efficient coupling was ensured by the interaction with a surface plasmon. They obtained a single-facet, single-mode cw output power of 2.4 W at a wavelength of 4.8 μm and $T = 298$ K (buried active region, 40 stages, cavity length of 5 mm, ridge width of 8 μm, high-reflection and antireflection coated facets, diamond submount). The side mode suppression ratio was 30 dB, and the continuous tuning range was 2084–2088 cm^{-1} at currents from 1 to 1.7 A. The far-field intensity distribution had one lobe.

Bai et al. [36] demonstrated a QCL with a record-high output power in pulsed mode. The laser design was the same as above, but the width of the active region was varied from 50 to 400 μm. In such a case, as a rule, several lasing channels develop (filamentation) because of optical inhomogeneity. In the case of QCLs, the filamentation problem is less significant because they have a near-zero linewidth enhancement factor. A multimode output power of 120 W was obtained from one laser facet in pulsed mode at an emission wavelength of 4.45 μm and $T = 298$ K (30 stages, cavity length of 3 mm, ridge width of 400 μm, epilayer-up on copper heatsink configuration).

Based on a strain-balanced $Ga_{0.27}In_{0.73}As/Al_{0.71}In_{0.29}As$ structure, researchers at Pranalytica developed QCLs for three wavelengths (3.5, 4.0 and 4.6 μm). They employed a more flexible electron extraction principle, which they named 'a nonresonant extraction design approach' [37]. In this approach, a radiative transition occurs between two levels, and the lower laser level is depopulated sequentially: first through resonant interaction with an LO phonon and then through bound to quasi-continuum scattering (Fig. 2a). A record-high cw output power at $T = 293$ K was achieved at an emission wavelength of 4.6 μm: the single-ended optical power of the laser (buried active region, cavity length of 5 mm, ridge width of 11.6 μm, high-reflection-coated back facet, antireflection-coated front facet, diamond submount) was 3 W (Fig. 8). The threshold current density was 0.86 A cm^{-2} and the wall plug efficiency was 12.7%. When the temperature was lowered to 80 K, 7.3 W of output power was obtained, which corresponded to an about 30% efficiency [38]. At an emission wavelength of 4 μm, the output power was however lower:

Table 2. Role of intervalley scattering in short-wavelength QCLs based on strained GaInAs/AlInAs heterostructures [37–40].

λ/μm	Pulsed mode (τ = 500 ns)		Continuous mode		Notes
	P/W	Efficiency (%)	P/W	Efficiency (%)	
3.6	0.3 (7 mm×8 μm)	–	0.05 (6 mm×6 μm)	–	The L and X valleys lie below the upper laser level; $T = 266$ K; 35 stages; $\tau = 300$ ns
4.0	2.18	10.5	0.75	5	The L and X valleys are identical in energy and lie 45 meV above the upper laser level; $T = 293$ K; 40 stages; 3.65 mm×8.7 μm
4.6	2 (AlN) 4.5 (diamond)	15.4	1.2 (AlN) 3 (diamond)	13	The L valley is 30 meV above the X valley and both lie above the upper laser level; $T = 293$ K; 30 stages; 3 mm×9.5 μm (AlN); 5 mm×15 μm (diamond)

Notes: The buried active region heterostructures were grown by molecular beam epitaxy. The table indicates the cavity length (mm) and ridge width (μm). The back facet was high-reflection-coated and the front facet was antireflection-coated. The laser chip was mounted episide down on an AlN or diamond submount.

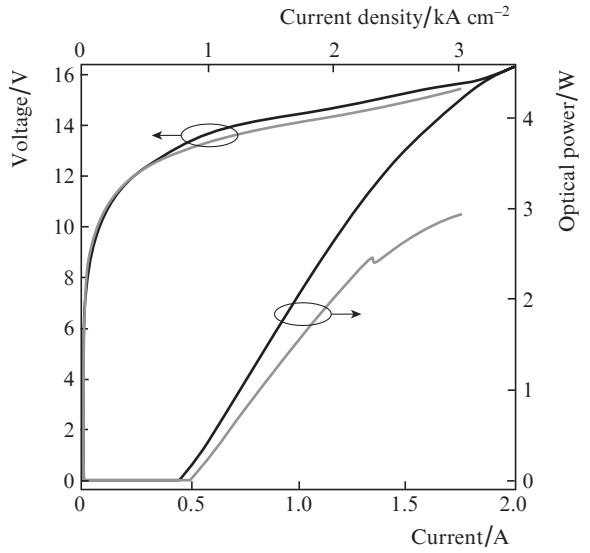

Figure 8. CW (gray curves) and pulsed (black curves) voltage–current and power–current characteristics of a nonresonant-extraction QCL at T = 293 K [37]. Buried active region heterostructure, antireflection-coated front facet, diamond submount, cavity length of 5 mm, stripe width of 11.6 μm.

0.75 and 2.18 W at T = 293 K in continuous and pulsed modes, respectively (Table 2).

When the heterostructure was designed to lase at 3.5 μm, the laser did not operate at room temperature even in pulsed mode. The average optical power in pulsed mode (duty cycle of 30%) at temperatures above 266 K was as low as 0.3 W. This result was explained [39, 40] by the fact that, with increasing emitted photon energy, intervalley scattering to the X and L side minima of the conduction band became more significant. At $h\nu$ = 0.27 eV (λ = 4.6 μm), the lowermost side minimum, X, is still 45 meV above the upper laser level. At $h\nu$ = 0.31 eV (λ = 4 μm), the two side minima and upper laser level differ little in energy. Finally, at $h\nu$ = 0.354 eV (λ = 3.5 μm) the side minima lie well below the upper laser level. This increases intervalley scattering and degrades the laser performance.

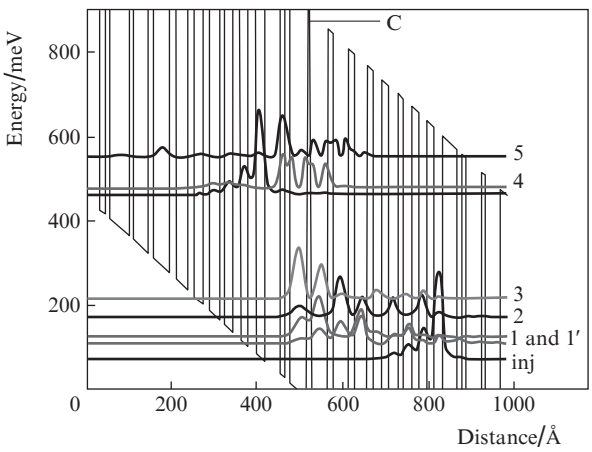

Figure 9. Active region band diagram for a nonresonant-extraction QCL based on a strained $Ga_{0.28}In_{0.72}As/In_{0.22}Al_{0.78}As$ structure; E = 93 kV cm^{-1} [45] (C = continuum, inj = injector ground level).

Thus, the short-wavelength limit of lasing in the GaInAs/AlInAs system lies near 4 μm even when the layers are strained. To shift the limit to shorter wavelengths, one should add antimony [24, 41–43], use high AlAs barriers [44] or change the material system.

A detailed study of the effect of layer composition and strain on the energy spectrum of heterostructures [37–40] made it possible to optimise the QCL design and achieve a record-high optical power. The latest Pranalytica's project is a QCL with a highly strained (~1%) active region and a tapered waveguide for beam outcoupling [45]. The laser operated in continuous mode at room temperature with an optical power above 4.5 W at a wavelength of 4.7 μm. Consider this encouraging result in greater detail.

Figure 9 shows the active region band diagram for a QCL based on a strained $Ga_{0.28}In_{0.72}As/In_{0.22}Al_{0.78}As$ structure. The QCL design with vertical optical transitions employs the nonresonant extraction design approach, which builds on the following principle [37]: In the case of completely resonant two-phonon depopulation of the lower laser level, the layer thicknesses in the active region are essentially fixed and are determined by resonance conditions and the 4 → 3 laser transition energy. In particular, the energy separation E_{54} is difficult to increase for parasitic current suppression because level 5 is located mostly in the same quantum wells as the lower energy levels 1 and 2. One way of imparting flexibility to the two-phonon design is by removing the resonance conditions for the energy spacings E_{32} and E_{21}, e.g. by slightly increasing the spacings relative to the phonon energy and creating a series of finite states (Fig. 2a). Even though the electron lifetime increases monotonically with increasing energy separation, the presence of several finite states allows the total lifetime to remain short.

The efficiency of injection to the upper laser level is usually thought to play a key role in determining the performance of short-wavelength QCLs. Thermal carrier leakage from the upper laser level 4 to the continuum states above the barriers reduces the population inversion in the laser at a given pump current density and, hence, increases the threshold current density. Another carrier leakage path is carrier excitation to level 5 followed by scattering to states other than level 4. The carrier leakage to the continuum states C and level 5 can be suppressed by increasing the energy spacings E_{C4} and E_{54} (Fig. 9). A straightforward way to increase E_{C4} is to increase the barrier height by using more highly strained $Ga_{1-x}In_xAs/In_yAl_{1-y}As$ structures. The use of higher barriers increases not only E_{C4} but also E_{54}, without changing the laser transition energy. Eventually, E_{C4} and E_{54} were increased from 230 and 63 meV in the old design to 420 and 72 meV, respectively, in the new design, as a result of the larger band offset at the higher strain. Therefore, the use of the compositions in question is attractive for suppressing the carrier leakage from the upper laser level.

Another advantage of the approach under consideration is that the energy of the X and L indirect valleys relative to the minimum of the Γ direct valley increases with strain. The carrier leakage from the upper laser level to the indirect valleys increases as the laser wavelength decreases to below 5 μm. Therefore, the performance of highly strained short-wavelength QCLs will be improved by suppressing the carrier leakage to the indirect valleys. At the same time, increasing the barrier height increases the laser transition linewidth.

The full width at high maximum of the EL line was just 22 meV (vertical transitions), attesting to excellent epitaxy quality in the highly strained structures. Typical thicknesses of the first and second barriers in the active region were as small as two to five monolayers (0.6 to 1.5 nm).

Note that, to achieve a high cw output power, a number of high-technology approaches were used in the laser design. The laser heterostructure was epitaxially buried, with a buried tapered waveguide for reducing the optical power density on the output facet. The cavity was 10 mm in length, with a ridge width of 7.5 μm in the central part and an output facet width of 20 μm. To improve heat removal conditions, the laser chip was mounted epi-down on an AlN/SiC composite submount using hard solder. The number of stages was increased to 40. The maximum wall plug efficiency of the laser was 16.3% at an optical power of 4 W. Reliability over 2000 h was demonstrated for an air-cooled system at a collimated beam power of 3 W and overall efficiency above 10%.

6. Laser efficiency

We consider here the wall plug efficiency, which is of greater practical interest. In the optimal case, the efficiency of QCLs usually reaches tens of percent at $T = 300$ K. The efficiency of the QCL designs under discussion, containing longitudinal optical phonon-assisted nonradiative transitions, cannot exceed 80% [46]. In view of this, two research groups [47, 48] aimed at reaching an efficiency of at least 50%. This would mean that most of the pump energy in their lasers was converted to radiation, and the rest, to heat.

Liu et al. [47] planned to reach high efficiency using efficient electron tunnelling injection into the active region. As shown in a previous theoretical study by Khurgin et al. [49], the injection process is limited by violations of the resonance tunnelling conditions because of the interface roughness induced detuning. To overcome this limitation, Liu et al. [47] realised a scheme with ultrastrong coupling between the injector ground level and upper laser level. In this scheme, the thickness of the injection barrier decreases from a typical 3–4 nm to 1 nm, increasing the splitting of the injector ground level and upper laser level from 2–4 to ~10 meV. The resulting strong coupling between the levels reduces the role of the interface and the Stark shift and improves the tuning of the levels in response to changes in bias. Moreover, the strong coupling between the injector and active region increases the 'penetration' of the upper laser level wave functions into the injector region, so that the radiative transitions become diagonal transitions and, as a result, the electron lifetime increases. Use was made of a three-well design. A strained $Ga_{0.34}In_{0.66}As/Al_{0.69}In_{0.31}As$ structure was grown by metalorganic vapour phase epitaxy (MOVPE). The active region was composed of 43 stages. The QCL operated at an emission wavelength of ~4.6 μm up to 300 K. The wall plug efficiency in pulsed mode at 160 K and lower temperatures was 40%–50%.

Another approach was adopted by Bai et al. [48]. Their design scheme was intended for low temperatures, and the injector was reduced to one doped quantum well. This allowed the voltage defect to be minimised because the energy separation between the level of the collector (merely the injector of the next stage) and the upper laser level was small but finite in order to prevent thermal backfilling of electrons. The laser design included three quantum wells, and the optical transition was almost vertical in order to maximise the internal quantum yield of emission. One obvious drawback to this design is that it is unsuitable for operation at elevated temperatures. Moreover, because of the small doped region, the applied electric field is very high (up to 1.5×10^5 V cm^{-1}). A strained $Ga_{0.34}In_{0.66}As/Al_{0.64}In_{0.36}As$ structure was grown by molecular beam epitaxy. The active region was composed of 70 stages. The QCL operated at an emission wavelength of ~5 μm up to 373 K. The wall plug efficiency in pulsed mode at 160 K and lower temperatures was 53%.

Thus, the above results [47, 48] demonstrate that the wall plug efficiency of QCLs can reach 50%, but this requires low operating temperatures and a large number of stages.

7. Operating life of QCLs

Advances in QCL development have been so great that such lasers are now being commercialised. In addition to university laboratories, about 20 companies focus on the growth of laser heterostructures, fabrication of QCLs and development of various QCL-based optical systems. Special mention should be given to Alpes Lasers, Pranalytica, Hamamatsu Photonics, Cascade Technologies, AdTech Optics Inc. and others. In this context, an important issue is the operating life of such lasers. To date, only strain-balanced AlInAs/GaInAs lasers (λ = 4.6–4.8 μm) have been life-tested. This system contains much indium, which prevents dislocation generation and propagation – processes that underlie the predominant semiconductor degradation mechanism. Researchers at Northwestern studied the voltage–current and power–current behaviour of a cw QCL (λ = 4.8 μm) at 298 K and a current slightly above threshold. The output power of the laser was 0.2–0.3 W. No significant changes in its performance parameters were detected over a period of 21 000 h (~2.4 years) [50]. Lyakh et al. [38] monitored the performance of a cw laser with an output power of 2.1 W (λ = 4.6 μm) at $T = 298$ K for 3560 h and detected no degradation. At $T = 80$ K, the laser operated for hundreds of hours, delivering a record-high optical power of 7.3 W.

Thus, even though the epilayers in the heterostructures of QCLs are strained (and their thickness is smaller than the critical thickness for misfit dislocation generation), the operating life of such lasers approaches 10^4 h or more, suggesting that large-scale QCL production is commercially viable.

8. Conclusions

The potentialities of modern QCL design development have not yet been exhausted, and the following trends can be outlined. To reduce the temperature dependence of the threshold current, one increases the energy separation between the upper laser level and the nearest higher energy states, up to the continuum, uses AlAs as a barrier material and increases the voltage defect, taking into account the scattering into the side valleys. Sb-containing solid solutions are used to produce barriers in short-wavelength QCLs. In AlInAs/GaInAs QCLs, lasing has been demonstrated in the range 3.3–24 μm. The short-wavelength limit of lasing in the InAs/AlSb system has been shifted to 2.6 μm. In the range $\lambda \sim 4.5$–4.7 μm, record-high optical powers have been obtained: up to 5–7 W in continuous mode and up to 120 W in pulsed mode. Wall plug efficiencies above 50% have been demonstrated at low temperatures. The unique feature of QCLs is the possibility to obtain a broad EL line (up to 600 cm^{-1}), which enables con-

tinuous frequency tuning of an individual mode in a range as broad as 400 cm^{-1} using an external dispersion cavity.

The QCL production process can be divided into four important steps: active region design simulation, laser heterostructure growth, postgrowth processing and characterisation. Special mention should be given to the epitaxial growth of multilayer nanoheterostructures (up to 1000 layers) with atomic layer accuracy. Molecular beam epitaxy has been and continues to be a basic method for the growth of such structures. As shown ten years after the advent of QCLs [51–53], high-quality laser heterostructures can also be grown by MOVPE, which opens up the possibility of commercial-scale production of such structures. The first QCLs produced in Russia lase at ~5 [54] and ~8 μm [4]. The former QCL was grown by molecular beam epitaxy, and the latter, by MOVPE.

Terahertz QCLs are beyond the framework of this paper. They are also unipolar devices but have their own distinctive features and require separate analysis. Note only the key advances made to date in the field of terahertz QCLs. Terahertz QCLs have been demonstrated with emission wavelengths in the range 67–250 μm (1.2–4.5 THz). Their operating temperature exceeds liquid-nitrogen temperature: 225 K in pulsed mode and under 117 K in continuous mode (at ~3 THz). The optical power obtained at an operating temperature of 5 K and a wavelength of ~70 μm is 0.25 W in pulsed mode and 0.14 W in continuous mode. Nonlinear optical methods developed for mid-IR QCLs are being adapted to the terahertz range.

Acknowledgements. This work was supported by the Russian Foundation for Basic Research (Grant Nos 11-02-00980-a and 11-02-12015-ofi-m-2011).

References

1. Kazarinov R.F., Suris R.A. Fiz. Tekh. Poluprovodn., **5**, 797 (1971).
2. Faist J., Capasso F., Sivco D.L., Sirtori C., Hutchinson A.L., Cho A.Y. *Science*, **264**, 553 (1994).
3. Gmachl C., Capasso F., Sivco D.L., Cho A.Y. *Rep. Prog. Phys.*, **64**, 1533 (2001).
4. Zasavitskii I.I., Pashkeev D.A., Marmalyuk A.A., Ryaboshtan Yu.L., Mikaelyan G.T. *Kvantovaya Elektron.*, **40**, 95 (2010) [*Quantum Electron.*, **40**, 95 (2010)].
5. Fujita K., Furuta S., Dougakiuchi T., Sugiyama A., Edamura T., Yamanishi M. *Opt. Express*, **19**, 2694 (2011).
6. Faist J., Hofstetter D., Beck M., Aellen T., Rochat M., Blaser S. *IEEE J. Quantum Electron.*, **38**, 533 (2002).
7. Wang Q.J., Pflügl C., Diehl L., Capasso F., Edamura T., Furuta S., Yamanishi M., Kan H. *Appl. Phys. Lett.*, **94**, 011103 (2009).
8. Scamarcio G., Capasso F., Sirtori C., Faist J., Hutchinson A.L., Sivco D.L., Cho A.Y. *Science*, **276**, 773 (1997).
9. Capasso F., Tredicucci A., Gmachl C., Sivco D.L., Hutchinson A.L., Cho A.Y., Scamarcio G. *IEEE J. Sel. Top. Quantum Electron.*, **5**, 792 (1999).
10. Tredicucci A., Capasso F., Gmachl C., Sivco D.L., Hutchinson A.L., Cho A.Y. *Appl. Phys. Lett.*, **73**, 2101 (1998).
11. Yang R.Q. *Superlattices Microstruct.*, **17**, 77 (1995).
12. Yang R.Q., Pei S.S. *J. Appl. Phys.*, **79**, 8197 (1996).
13. Canedy C.L., Bewley W.W., Lindle J.R., Kim C.S., Kim M., Vurgaftman I., Meyer J.R. *Appl. Phys. Lett.*, **88**, 161103 (2006).
14. Vurgaftman I., Bewley W.W., Canedy C.L., Kim C.S., Kim M., Lindle J.R., Merritt C.D., Abell J., Meyer J.R. *IEEE J. Sel. Top. Quantum Elrectron.*, **17**, 1435 (2011).
15. Bewley W.W., Canedy C.L., Kim C.S., Kim M., Merritt C.D., Abell J., Vurgaftman I., Meyer J.R. *Opt. Express*, **20**, 3235 (2012).
16. Yang R.Q., Bruno J.D., Bradshaw J.L., Pham J.T., Wortman D.E. *Physica E*, **7**, 69 (2000).
17. Huang X., Charles W.O., Gmachl C. *Opt. Express*, **19**, 8297 (2011).
18. Hofstetter D., Beck M., Aellen T., Faist J. *Appl. Phys. Lett.*, **78**, 396 (2001).
19. Faist J., Beck M., Aellen T., Gini E. *Appl. Phys. Lett.*, **78**, 147 (2001).
20. Fujita K., Furuta S., Sugiyama A., Ochiai T., Edamura T., Akikusa N., Yamanishi M., Kan H. *Appl. Phys. Lett.*, **91**, 141121 (2007).
21. Botez D., Kumar S., Shin J.C., Mawst L.J., Vurgaftman I., Meyer J.R. *Appl. Phys. Lett.*, **97**, 071101 (2010).
22. Bai Y., Bandyopadhyay N., Tsao S., Selcuk E., Slivken S., Razeghi M. *Appl. Phys. Lett.*, **97**, 251104 (2010).
23. Fujita K., Yamanishi M., Edamura T., Sugiyama A., Furuta S. *Appl. Phys. Lett.*, **97**, 201109 (2010).
24. Cathabard O., Teissier R., Devenson J., Moreno J.C., Baranov A.N. *Appl. Phys. Lett.*, **96**, 141110 (2010).
25. Colombelli R., Capasso F., Gmachl C., Hutchinson A.L., Sivco D.L., Tredicucci A., Wanke M.C., Sergent A.M., Cho A.Y. *Appl. Phys. Lett.*, **78**, 2620 (2001).
26. Wittmann A., Bonetti Y., Fischer M., Faist J., Blaser S., Gini E. *IEEE Photonics Technol. Lett.*, **21**, 814 (2009).
27. Hugi A., Maulini R., Faist J. *Semicond. Sci. Technol.*, **25**, 083001 (2010).
28. Gmachl C., Sivco D.L., Colombelli R., Capasso F., Cho A. *Appl. Phys. Lett.*, **79**, 572 (2001).
29. Gmachl C., Sivco D.L., Baillargeon J.N., Hutchinson A.L., Capasso F., Cho A.Y. *Nature*, **415**, 883 (2002).
30. Wysocki G., Lewicki R., Curl R.F., Tittel F.K., Diehl L., Capasso F., Troccoli M., Hofler G., Bour D., Corzine S., Maulini R., Giovanni M., Faist J. *Appl. Phys. B*, **92**, 305 (2008).
31. Hugi A., Terazzi R., Bonetti Y., Wittmann A., Fischer M., Beck M., Faist J., Gini E. *Appl. Phys. Lett.*, **95**, 061103 (2009).
32. Yao Y., Wang X., Fan J.-Y., Gmachl C.F. *Appl. Phys. Lett.*, **97**, 081115 (2010).
33. Fujita K., Furuta S., Sugiyama A., Ochiai T., Ito A., Dougakiuchi T., Edamura T., Yamanishi M. *Appl. Phys. Lett.*, **98**, 231102 (2011).
34. Bai Y., Bandyopadhyay N., Tsao S., Slivken S., Razeghi M. *Appl. Phys. Lett.*, **98**, 181102 (2011).
35. Lu Q.Y., Bai Y., Bandyopadhyay N., Slivken S., Razeghi M. *Appl. Phys. Lett.*, **98**, 181106 (2011).
36. Bai Y., Slivken S., Darvish S.R., Haddadi A., Gokden B., Razeghi M. *Appl. Phys. Lett.*, **95**, 221104 (2009).
37. Lyakh A., Maulini R., Tsekoun A., Go R., Pflügl C., Diehl L., Wang Q.G., Capasso F., Patel C.K.N. *Appl. Phys. Lett.*, **95**, 141113 (2009).
38. Lyakh A., Maulini R., Tsekoun A.G., Patel C.K.N. *Opt. Eng.*, **49**, 111105 (2010).
39. Lyakh A., Maulini R., Tsekoun A.G., Go R., Patel C.K.N. *Proc. SPIE Int. Soc. Opt. Eng.*, **7953**, 79531L (2011).
40. Tsekoun A.G., Lyakh A., Maulini R., Lane M., Macdonald T., Go R., Patel C.K.N. *Proc. SPIE Int. Soc. Opt. Eng.*, **7325**, 73250L (2009).
41. Yang Q., Manz C., Bronner W., Köhler K., Wagner J. *Appl. Phys. Lett.*, **88**, 121127 (2006).
42. Commin J.P., Revin D.G., Zhang S.Y., Krysa A.B., Kennedy K., Cockburn J. *Appl. Phys. Lett.*, **97**, 031108 (2010).
43. Revin D.G., Zhang S.Y., Commin J.P., Kennedy K., Krysa A.B., Cockburn J. *IEEE Photonics Technol. Lett.*, **22**, 757 (2010).
44. Bismuto A., Beck M., Faist J. *Appl. Phys. Lett.*, **98**, 191104 (2011).
45. Lyakh A., Maulini R., Tsekoun A., Go R., Patel C.K.N. *Opt. Express*, **20**, 4382 (2012).
46. Faist J. *Appl. Phys. Lett.*, **90**, 253512 (2007).
47. Liu P.Q., Hoffman A.J., Escarra M.D., Franz K.J., Khurgin J.B., Dikmelik Y., Wang X., Fan J.-Y., Gmachl C.F. *Nat. Photonics*, **4**, 95 (2010).

48. Bai Y., Slivken S., Kuboya S., Darvish S.R., Razeghi M. *Nat. Photonics*, **4**, 99 (2010).
49. Khurgin J.B., Dikmelik Y., Liu P.Q., Hoffman A.J., Escarra M.D., Franz K.J., Gmachl C.F. *Appl. Phys. Lett*., **94**, 091101 (2009).
50. Razeghi M. *New J. Phys*., **11**, 125017 (2009).
51. Roberts J.S., Green R.P., Wilson L.R., Zibik E.A., Revin D.G., Cockburn J.W., Airey R.J. *Appl. Phys. Lett*., **82**, 4221 (2003).
52. Krysa A.B., Roberts J.S., Green R.P., Wilson L.R., Page H., Garsia M., Cockburn J.W. *J. Cryst. Growth*, **272**, 682 (2004).
53. Bour D., Troccoli M., Capasso F., Corzine S., Tandon A., Mars D., Höfler G. *J. Cryst. Growth*, **272**, 526 (2004).
54. Mamutin V.V., Ustinov V.M., Boetthchner J., Kuenzel H. *Pis'ma Zh. Tekh. Fiz*., **36**, 34 (2010).